nanomaterials

MDPI

Article

Optical Interference and Spectral Thermal Emission in Nanometric Multilayer Coatings: Effects on Admissible Thermal Loads of Nickel-Based Superalloys

Liviu Badea [1,†,*] and Mirela Dragan [1,†,*]

Supplementary Material

This Supplementary Material collects the auxiliary relations, the Monte Carlo priors, the structural variants and three supplementary figures. Equations, figures and tables carry the prefix S; unprefixed numbers refer to the main text, and reference numbers are those of the main reference list.

S1. Monte Carlo priors and structural variants

Table S1 lists the 15 independent factors of the Monte Carlo analysis, all sampled from uniform distributions. Most intervals are assumptions chosen to cover plausible values; their basis is given in the last column.

Table S1. Uniform priors of the 15 Monte Carlo factors (one-dimensional reduced model).

Parameter	Symbol	Range	Unit	Basis
Bond-coat damping, Wiedemann–Franz prior (wide prior)	γ_{bc}	2469–3434 (1500–7000)	cm^{-1}	WF interval with [29]; assumption
Metal plasma wavenumber	$\tilde{\nu}_p$	32 000–41 500	cm^{-1}	Assumption around [28]
Metal background permittivity	ε_{bg}	1–5	–	Assumption
HEO-Z bulk reflectance minimum (sets $\Delta\varepsilon$)	$\tilde{\nu}_{min}$	710–720	cm^{-1}	Model choice; cf. [26]
HEO-Z damping ratio	g_{300}	0.025–0.25	–	Assumption
HEO-Z mode-shift coefficient	b_Ω	$(2.4–3.9) \times 10^{-5}$	K^{-1}	Corundum mode trends [23]
HEO-Z damping coefficient	b_γ	$(1.3–6.4) \times 10^{-3}$	K^{-1}	Corundum mode trends [23]
Scale of the Al_2O_3 extrapolation above 928 K	a_{ext}	0.5–1.5	–	Assumption
Thermal conductivity HEO-Z	k_1	0.8–2.0	$W\ m^{-1}\ K^{-1}$	Assumption [6]
Thermal conductivity Al_2O_3	k_2	5–10	$W\ m^{-1}\ K^{-1}$	Assumption [32]
Boundary resistance HEO-Z/Al_2O_3	R_1	1×10^{-9}–1×10^{-8}	$m^2\ K\ W^{-1}$	Assumption [11]
Boundary resistance Al_2O_3/NiCrAlY	R_2	2×10^{-9}–1×10^{-7}	$m^2\ K\ W^{-1}$	Assumption [11,34]
Boundary resistance NiCrAlY/Nimonic 80A	R_3	2.5×10^{-10}–1×10^{-9}	$m^2\ K\ W^{-1}$	Assumption [10]
Scale factor of the Nimonic 80A conductivity	k_{Nim}	0.85–1.15	–	Assumption around [30]
Back-face emissivity	ε_{back}	0.3–0.9	–	Assumption

 https://doi.org/10.3390/nano16231561

The structural variants of Table S2 change a modeling choice rather than a parameter value. They have no probability distribution and are therefore reported as one-at-a-time changes of the admissible loads, not combined with the Monte Carlo bands of Table 3.

Table S2. Structural variants, applied one at a time, and their effect on the admissible loads.

Structural variant	Effect on the admissible load (one-dimensional unless stated)
Gray rim ($\varepsilon_{rim} = 0.6$) instead of adiabatic rim (two-dimensional)	S1-L +6.6 %; S2-L +5.8 %; S2-B +0.2 %; S3-L +29.8 %
Graded interfaces, Bruggeman layer of thickness 2σ, $\sigma = 20$ nm	S3-L −34.9 %; S2 ≤ 0.9 %
Névot–Croce attenuation, $\sigma = 20$ nm	S3-L −12.8 %
Nickel interband terms in both metals	S3-L −30.4 % (hemispherical absorptance); about −32 % at normal incidence; S2 < 1 %
Pure FPSQ Al_2O_3 wing instead of causal blend	S3-L −8.3 %; S1-L −2.2 %
Switch parameters of the Al_2O_3 wing	−0.24 % to +0.12 %
Al_2O_3 anisotropy (ordinary, extraordinary, uniaxial, Bruggeman)	≤ 0.7 %
Al_2O_3 optical extrapolation above 928 K	≤ 0.24 %
No interior radiation at the BC-B back face	S1-B −0.64 %; S2-B −0.12 %; S3-B −2.55 %
Non-isothermal emission of the resolved coating (bound Ξ)	$\leq 3 \times 10^{-6}$
Coating conductivities and boundary resistances	≤ 0.006 %
Incoherent Al_2O_3 layer (phase averaging; limiting case only)	$\varepsilon_h - 0.04$
Lorenz number 2.79×10^{-8} W Ω K^{-2} instead of L_0	γ_{bc} +14 %, inside the wide prior of Table S1

S2. Auxiliary relations

The relations below are standard. They are listed because they fix the treatment of the spectral tails, the roughness variants and the variance-based sensitivity indices.

The Planck power outside the spectral grid is added analytically. With $x = hc \cdot 100\tilde{\nu}/(k_B T)$, the fraction of the blackbody emissive power above x is, for $x \geq 1$, given by the rapidly convergent series

$$F_{>}(x) = \frac{15}{\pi^4} \sum_{n=1}^{\infty} \mathrm{e}^{-nx} \left(\frac{x^3}{n} + \frac{3x^2}{n^2} + \frac{6x}{n^3} + \frac{6}{n^4} \right), \tag{S1}$$

which follows from term-by-term integration of the Planck function written as a geometric series in e^{-x}. For $x < 1$ the complementary fraction $1 - F_{>}$ is evaluated from the Bernoulli-number expansion of the incomplete integral, which converges for $x < 2\pi$. Both tails are added to the grid integral in Equation (7) with the emissivity held at its value at the grid edge, so the normalization by σT^4 is exact up to the truncation of the series.

The first roughness variant of Section 3.9 replaces each interface by a graded layer of thickness 2σ with equal volume fractions $f_i = 1/2$ of the two adjacent materials, whose permittivity ε_{eff} follows from the Bruggeman condition [47]

$$\sum_i f_i \frac{\varepsilon_i - \varepsilon_{\mathrm{eff}}}{\varepsilon_i + 2\varepsilon_{\mathrm{eff}}} = 0, \tag{S2}$$

https://doi.org/10.3390/nano16231561

with the root of positive imaginary part. The second variant keeps the interfaces sharp and attenuates the Fresnel coefficients entering Equation (4) by the Névot–Croce factor [46],

$$\tilde{r}_{j,j+1} = r_{j,j+1}\exp\left(-2k_{z,j}k_{z,j+1}\sigma^2\right), \tag{S3}$$

where σ is the root-mean-square roughness. Equation (S2) assumes quasi-static spherical inclusions and Equation (S3) a Gaussian height distribution with lateral scales larger than the wavelength. The two variants describe different interface structures and are not part of the Monte Carlo sampling.

Total Sobol indices are estimated from two independent sample matrices **A** and **B** of size $N \times k$ and the matrices $\mathbf{A}_B^{(i)}$, in which column i of **A** is replaced by that of **B**, with the Jansen estimator [41,42]

$$S_{T,i} = \frac{1}{2N\,V(Y)}\sum_{n=1}^{N}\left[f(\mathbf{A})_n - f(\mathbf{A}_B^{(i)})_n\right]^2, \tag{S4}$$

where f is the admissible load of the reduced one-dimensional model and $V(Y)$ the variance of the pooled outputs $f(\mathbf{A})$ and $f(\mathbf{B})$. The estimator requires $N(k+2)$ model evaluations and assumes independent inputs, which holds for the priors of Table S1. With $N = 128$ and $k = 8$ its sampling error on analytic benchmarks is 0.05–0.14, which also explains estimates slightly above 1 for a dominant factor. The standard error of the Monte Carlo mean is

$$\mathrm{SE}(\bar{P}) = \frac{s_P}{\sqrt{N}}, \tag{S5}$$

with s_P the sample standard deviation of independent samples; this rate is used to check the convergence shown in Figure S3c.

S3. Supplementary figures

The p-polarized emissivity approaches unity near 11 μm (Figure S1a), with the grid maximum at about 52°, on the ridge discussed with Figure 5. Although the hemispherical weight $2\cos\theta\sin\theta$ at 52° is within 3 % of its maximum, the ridge adds little to ε_h, because less than a tenth of the emitted power lies above 10 μm at the cap (Figure 4c). Figure S1b varies only the HEO-Z thickness d_1. A thicker film shifts the interference orders to longer wavelengths and adds new orders at short wavelengths, while the Al_2O_3 features near 18–20 μm stay in place, as expected for bulk phonon absorption. At the nominal $d_1 = 200$ nm only a few orders fall inside the Planck band, so ε_h is set by the positions of individual maxima rather than by an average over many. (Figure S1c) is not an independent three-dimensional simulation: it is the axisymmetric solution $T(r, z)$ of S2-L at its two-dimensional admissible gas temperature, rotated about the axis. The field varies by about 11 K, with the maximum at the center of the coated face. About 5 K of this spread is the axial drop qL/k across the 2 mm substrate, and the rest is the radial nonuniformity created by the gray rim (Section 3.8). The thickness map (Figure S1d) covers $d_1 = 0$–1000 nm and $d_2 = 0$–1500 nm. Its lower-left corner reproduces the bare metal ($\varepsilon_h \approx 0.14$), and the steepest gradients occur for thin stacks, in which the first order sweeps through the band that carries most of the emitted power. The baseline lies on a broad plateau, so thickness deviations of about 100 nm change ε_h only weakly. The largest ε_h, about 0.26 against 0.21 for the baseline, lies on the boundary $d_2 = 0$, without alumina, and would raise the admissible gas temperature of S2-L by less than 15 K. At this point, $d_1 \approx 400$ nm, the quarter-wave estimate of the first order, $4n_1d_1 \approx 3.4$ μm, falls inside the 2–5 μm band that carries about half of the emitted power. It is a maximum on the searched grid, not a design optimum, because it removes the alumina scale that the system requires

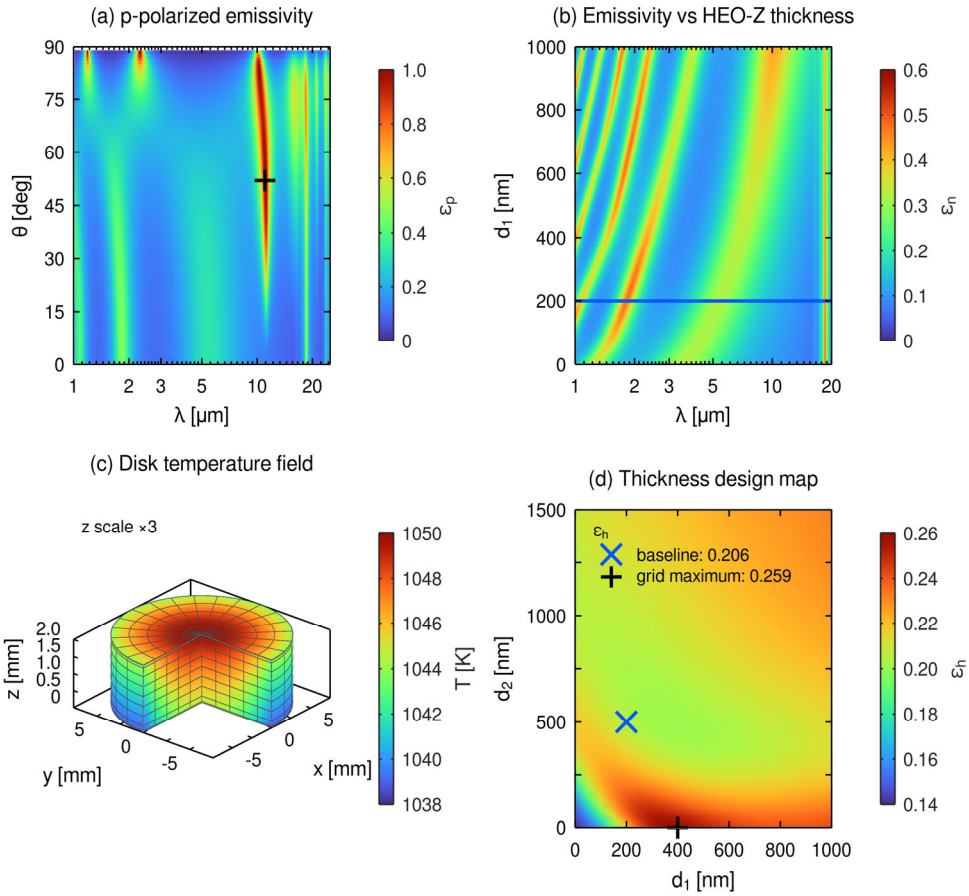

Figure S1. Supplementary optical results and temperature field (γ_{bc} = 3018 cm^{-1}, 1050 K). (a) *p*-polarized emissivity $\varepsilon_p(\lambda, \theta)$; marker: grid maximum. (b) Normal emissivity versus λ and d_1 (d_2 = 500 nm, d_3 = 200 nm); line: nominal d_1. (c) Temperature field of S2-L at the two-dimensional $T_{g,adm}$, reconstructed by rotating the axisymmetric solution (axial scale ×3, one quarter removed, coating not drawn). (d) ε_h versus d_1 and d_2; markers: baseline (legend B0) and grid maximum (legend "optimum").

For a steady composite wall with three boundary resistances, the finite-volume temperatures reproduce the exact piecewise-linear solution to round-off (Figure S2a); since the scheme is exact for linear profiles, this checks the assembly of conductances and interface resistances. For a slab with one convective face (Bi = hL/k = 1) and one insulated face, $\theta = (T - T_\infty)/(T_0 - T_\infty)$ follows the Carslaw–Jaeger series [37] versus Fo = $\alpha t/L^2$ within a few 10^{-6} (Figure S2b). In Figure S2c the spatial order 2 is measured against the series and the orders 1 and 2 of implicit Euler and Crank–Nicolson from successive step halvings. Neither scheme is used in production. The variable-step BDF2 scheme was verified separately against the same series, with order 2.0 for uniform and graded steps. The two-dimensional model with an adiabatic rim reproduces the one-dimensional history to round-off (Figure S2d). The resolved and reduced coating models differ by less than 0.1 K in the transient and by at most about 11 mK at steady state. This difference is not a heat-capacity effect, since storage vanishes at steady state. The resolved model deposits the net radiative exchange in the metal skin below the transparent oxides, which then carry the conducted flux minus the net absorbed radiation, whereas the reduced model routes the whole flux through the oxide resistance. The predicted shift matches the computed one within 3 mK.

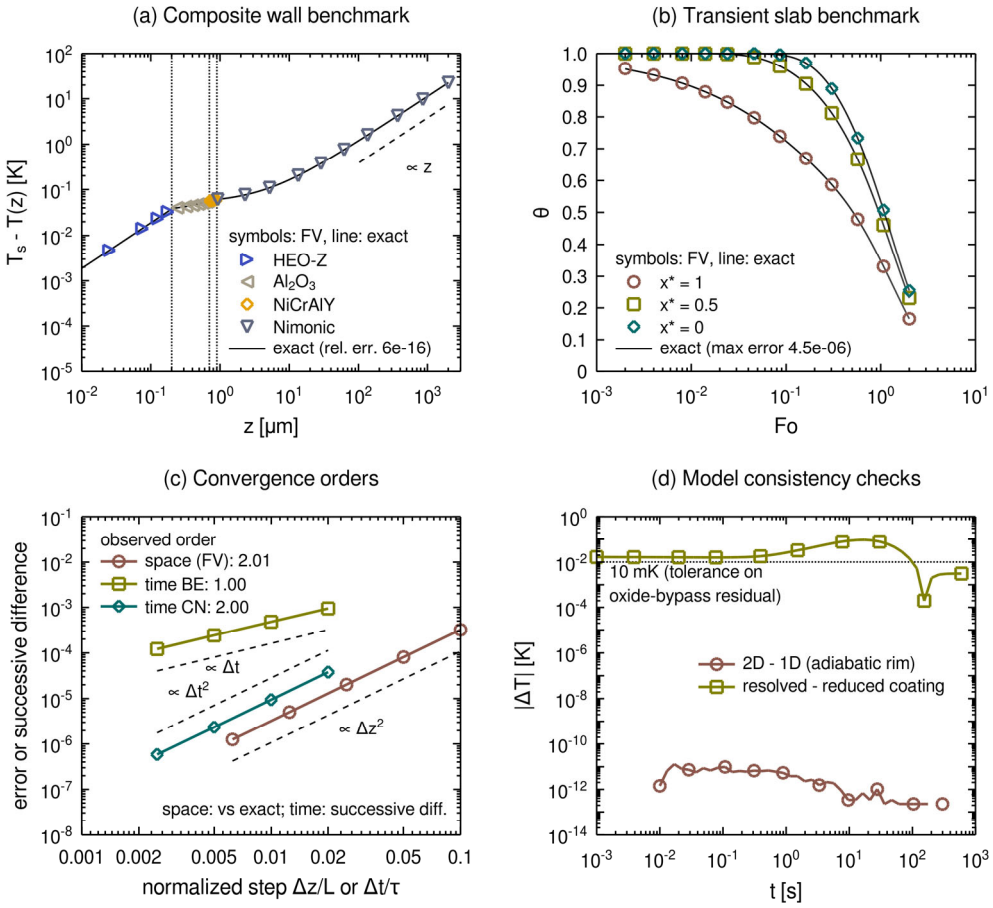

Figure S2. Verification of the conduction solver. (a) Steady composite wall: $T_s - T(z)$ (symbols: finite volumes; line: exact). (b) Slab with Bi = 1: θ versus Fo at three positions, with the series solution. (c) Spatial error and successive temporal differences for implicit Euler (BE) and Crank–Nicolson (CN); legend: observed orders. (d) $|\Delta T|$ between the two- and one-dimensional models (adiabatic rim) and between the resolved and reduced coatings; dotted: 10 mK, the tolerance applied to the residual of the oxide-bypass prediction.

The Monte Carlo results depend on the priors of Table S1, which are assumed intervals, not measured distributions. Two priors for the bond-coat damping are compared: the Wiedemann–Franz prior, based on the Sommerfeld Lorenz number, and a wide prior that admits departures from it. With the first, the distribution of the admissible gas temperature of S2-L is about a fifth narrower (Figure S3a), and interband terms shift it without widening it. Figure S3(b) gives the probability of exceeding the cap, conditional on the assumed distributions; it is not an observed failure frequency. A 1 % probability requires a back-off of a few percent for S1-L and S2-L, almost none for S2-B and about a quarter for S3-L. The standard error of the mean decreases as $N^{-1/2}$ (Equation (S5)) and falls below 1 K at N = 2000 (Figure S3c); this rate does not certify the tails or the Sobol indices, which converge more slowly. The total Sobol indices (Figure S3d) identify the back-face emissivity as the dominant factor for S2-L under both priors, and the bond-coat damping as second with the wide prior. The intervals of the other factors overlap, so we do not rank them. The dominant index exceeds 1 by less than its sampling error; an exact total index cannot exceed 1, so the excess is an estimation artifact.

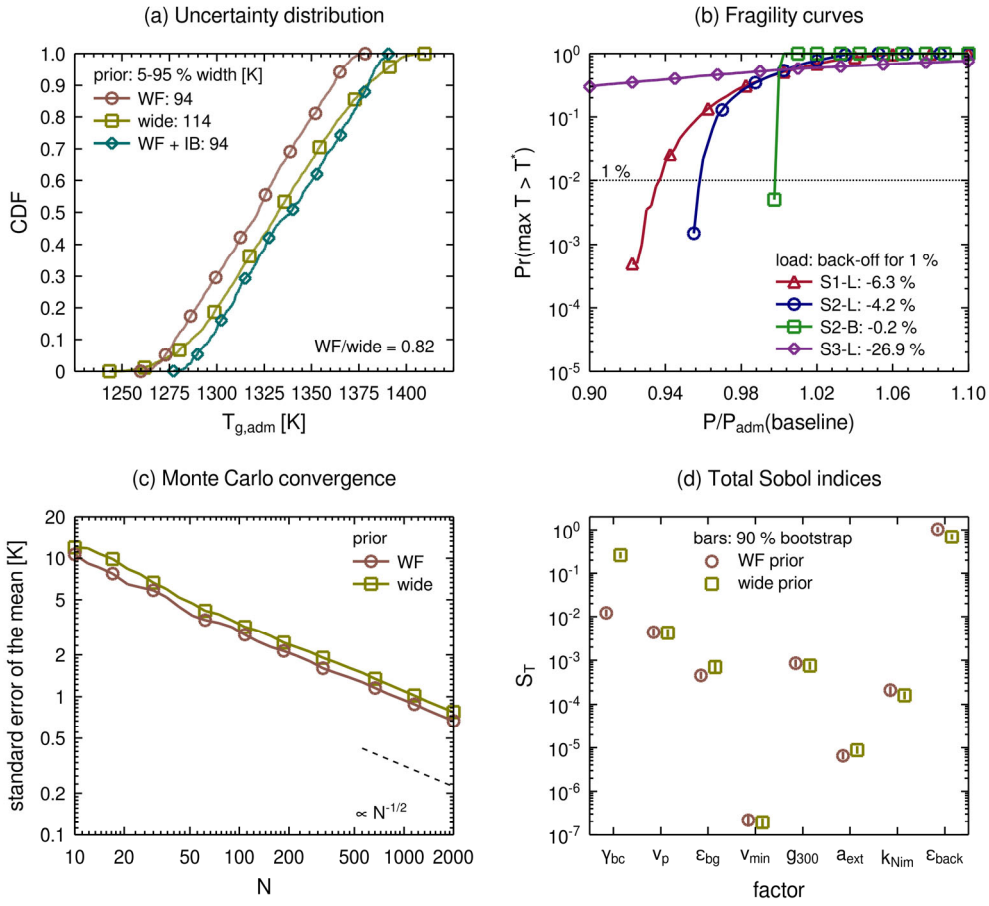

Figure S3. Uncertainty analysis (one-dimensional reduced model). (a) Cumulative distribution of $T_{g,adm}$ (S2-L) for the Wiedemann–Franz (WF, labelled v2) and wide (labelled v1) priors (2000 samples each) and WF with interband terms (500 samples); legend: 5–95 % widths. (b) Probability, conditional on Table S1, that the maximum temperature exceeds T^* versus the load normalized by the baseline admissible load of the reduced model (label B0′, distinct from the baseline stack B0 of Figure S1). (c) Standard error of the mean versus N. (d) Total Sobol indices of eight factors for S2-L (Jansen, base sample 128; bars: 90 % bootstrap intervals).

References

6. Liu, D.; Shi, B.; Geng, L.; Wang, Y.; Xu, B.; Chen, Y. High-entropy rare-earth zirconate ceramics with low thermal conductivity for advanced thermal-barrier coatings. *J. Adv. Ceram.* **2022**, *11*, 961. https://doi.org/10.1007/s40145-022-0589-z.
10. Gundrum, B.C.; Cahill, D.G.; Averback, R.S. Thermal conductance of metal-metal interfaces. *Phys. Rev. B* **2005**, *72*, 245426. https://doi.org/10.1103/PhysRevB.72.245426.
11. Blank, M.; Weber, L. Towards a coherent database of thermal boundary conductance at metal/dielectric interfaces. *J. Appl. Phys.* **2019**, *125*, 095302. https://doi.org/10.1063/1.5085176.
23. Zeidler, S.; Posch, T.; Mutschke, H. Optical constants of refractory oxides at high temperatures. *Astron. Astrophys.* **2013**, *553*, A81. https://doi.org/10.1051/0004-6361/201220459.
26. Pecharromán, C.; Ocaña, M.; Serna, C.J. Optical constants of tetragonal and cubic zirconias in the infrared. *J. Appl. Phys.* **1996**, *80*, 3479. https://doi.org/10.1063/1.363218.
28. Ordal, M.A.; Bell, R.J.; Alexander, R.W.; Long, L.L.; Querry, M.R. Optical properties of fourteen metals in the infrared and far infrared: Al, Co, Cu, Au, Fe, Pb, Mo, Ni, Pd, Pt, Ag, Ti, V, and W. *Appl. Opt.* **1985**, *24*, 4493. https://doi.org/10.1364/AO.24.004493.
29. Raj, S.V. *Thermophysical Properties of Cold and Vacuum Plasma Sprayed Cu-Cr-X Alloys, NiAl and NiCrAlY Coatings, Part 1: Electrical and Thermal Conductivity, Thermal Diffusivity, and Total Hemispherical Emissivity*; NASA/TM-2017-219715; NASA Glenn Research Center: Cleveland, OH, USA, 2017. Available online: https://ntrs.nasa.gov/api/citations/20170011293/downloads/20170011293.pdf.

30. Special Metals Corporation. *NIMONIC Alloy 80A*; Publication No. SMC-099; Special Metals Corporation: Huntington, WV, USA, 2004. Available online: https://www.specialmetals.com/documents/technical-bulletins/nimonic-alloy-80A.pdf.
32. Munro, R.G. Evaluated material properties for a sintered α-alumina. *J. Am. Ceram. Soc.* **1997**, *80*, 1919–1928. Available online: https://srdata.nist.gov/CeramicDataPortal/Pds/Scdaos (accessed on 9 November 2026).
34. Cappella, A.; Battaglia, J.-L.; Schick, V.; Kusiak, A.; Lamperti, A.; Wiemer, C.; Hay, B. High temperature thermal conductivity of amorphous Al_2O_3 thin films grown by low temperature ALD. *Adv. Eng. Mater.* **2013**, *15*, 1046. https://doi.org/10.1002/adem.201300132.
37. Carslaw, H.S.; Jaeger, J.C. *Conduction of Heat in Solids*, 2nd ed.; Clarendon Press: Oxford, UK, 1959.
41. Saltelli, A.; Annoni, P.; Azzini, I.; Campolongo, F.; Ratto, M.; Tarantola, S. Variance based sensitivity analysis of model output. Design and estimator for the total sensitivity index. *Comput. Phys. Commun.* **2010**, *181*, 259. https://doi.org/10.1016/j.cpc.2009.09.018.
42. Jansen, M.J.W. Analysis of variance designs for model output. *Comput. Phys. Commun.* **1999**, *117*, 35. https://doi.org/10.1016/S0010-4655(98)00154-4.
46. Névot, L.; Croce, P. Caractérisation des surfaces par réflexion rasante de rayons X. Application à l'étude du polissage de quelques verres silicates. *Rev. Phys. Appl.* **1980**, *15*, 761. https://doi.org/10.1051/rphysap:01980001503076100.
47. Bruggeman, D.A.G. Berechnung verschiedener physikalischer Konstanten von heterogenen Substanzen. I. Dielektrizitätskonstanten und Leitfähigkeiten der Mischkörper aus isotropen Substanzen. *Ann. Phys.* **1935**, *416*, 636. https://doi.org/10.1002/andp.19354160705.

Disclaimer/Publisher's Note: The statements, opinions and data contained in all publications are solely those of the individual author(s) and contributor(s) and not of MDPI and/or the editor(s). MDPI and/or the editor(s) disclaim responsibility for any injury to people or property resulting from any ideas, methods, instructions or products referred to in the content.